Verification of the Sensitivity of Direction-Dependent Light Detection for the NIR Absorption Imaging Problem

F. H. Schlereth[1], R. L. Barbour[2,3], H. L. Graber[2]

1) Department of Electrical and Computer Engineering, 2-189 CST, Syracuse University, Syracuse, NY 13244

2)Departments of Physiology and Biophysics, and 3) Pathology, SUNY Health Science Center at Brooklyn, 450 Clarkson Avenue, Brooklyn, NY 11203

1.0 BACKGROUND and INTRODUCTION

The bulk of our work on imaging the spatial distribution of NIR absorption in biological tissue has employed various perturbation methods for the image reconstructions[1-3]. In the last two years, members of our group, under the direction of F. H. Schlereth, have also been actively investigating the use of neural net algorithms for this purpose[4]. A block diagram illustrating all the essential features of the algorithm used is shown in Figure 1.

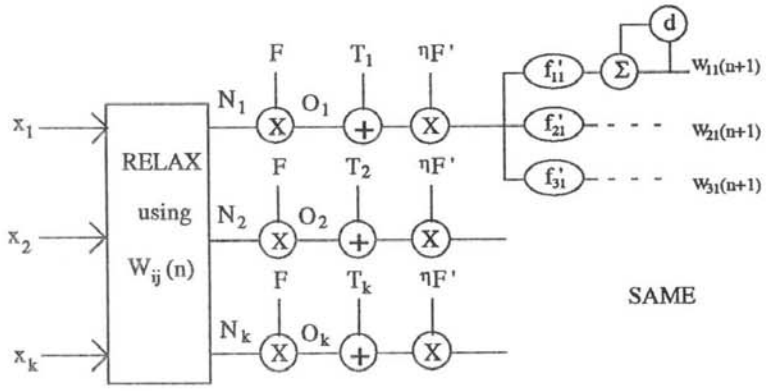

FIGURE 1 Block diagram of neural net for image reconstruction (reprinted from reference 4). The $w_{ij}(n)$'s calculated at the end of each cycle are fed back into the relaxation solver for the next update of the forward problem. This is a neural net implementation of a gradient descent algorithm[5] that minimizes the mean squared error $E = \sum_k (T_k - O_k)^2$. Symbols denote: x_i = energy put into the medium by the i^{th} source; $w_{ij}(n)$ = absorption estimate for the cell at position ij in iteration n; N_i = i^{th} calculated light output; F= activation function; O_i = i^{th} output following activation, T_i = i^{th} component of training vector (physical measurement of light angular flux, in this case); η = gain constant; F' = derivative of activation function; f'_{ij} is the total flux in cell ij of the medium. Circled "X," "+," and "Σ" denote multiplication, addition, and summation operations, respectively; circled "d" is a delay loop in which the previous value of f'_{ij} is stored. For small changes in w_{ij}, $\Delta E \propto (\Delta w_{ij})^2$.

An important lesson of our first round of image reconstruction by this method is the importance of preprocessing operations, *i.e.*, making use of information from sources *other than* the intensity- or flux-measurement data to restrict the set of possible solutions. This is illustrated in Figure 2, which shows the absorption distribution of one specimen medium and the results of two different image reconstructions. Because there were fewer flux measurements than unknowns, the problem is underdetermined and it is important to note that the "solution" in the middle panel satisfies the requirements of all the detector readings even though it bears no physical resemblance to the target. The result shown in the third panel is much more physically accurate, despite the fact that the medium in this case scattered light isotropically, and this would therefore be expected to be a more difficult reconstruction than for the case of the forward-directed scattering (g = 0.610) modeled in the previous case. The reason this reconstruction was more successful is that *a priori* information about the

0-8194-1114-0/93/$6.00

medium was incorporated into the algorithm; in essence, the neural net was told it should adjust its estimate of absorption strength in cells near the center first.

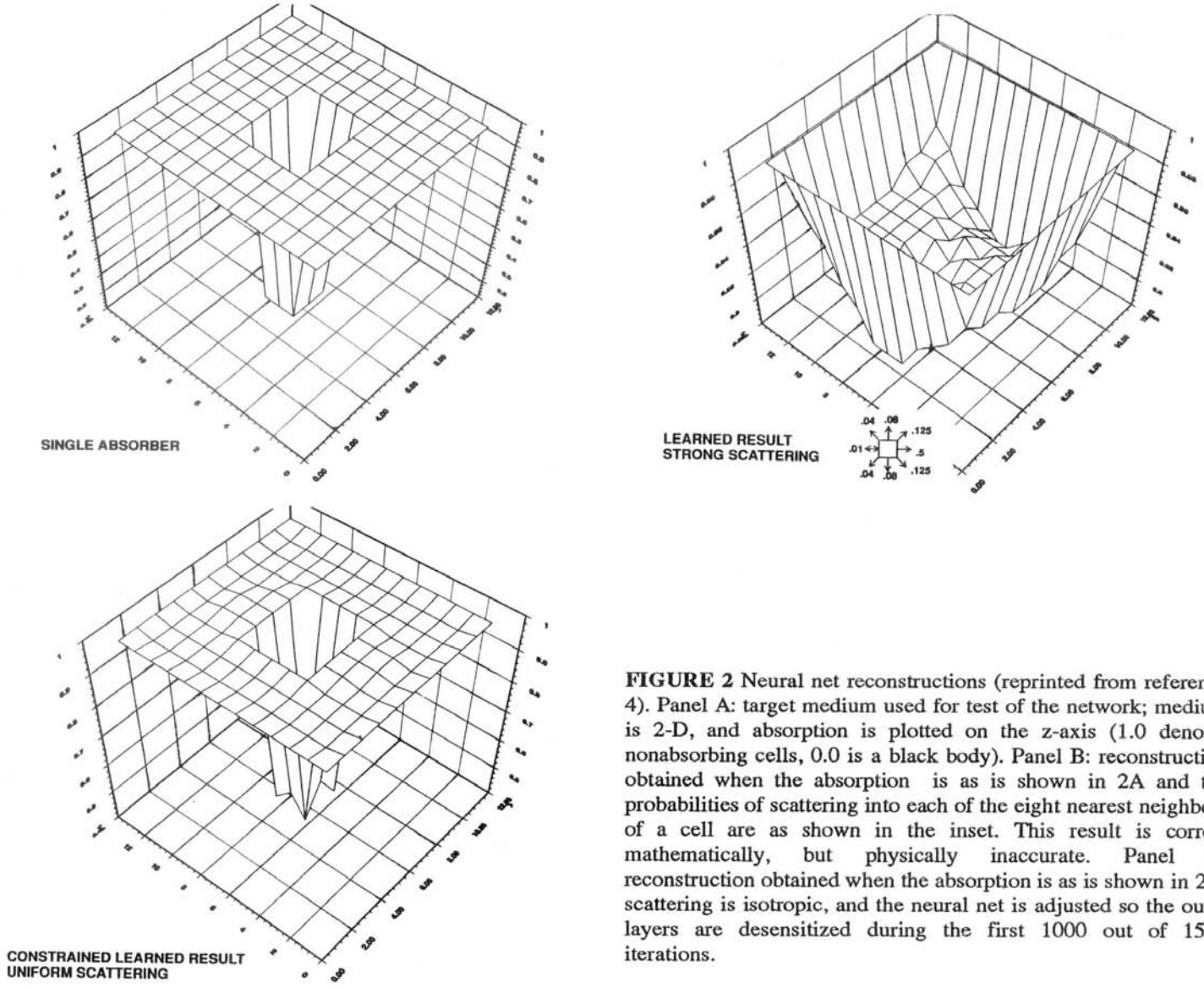

FIGURE 2 Neural net reconstructions (reprinted from reference 4). Panel A: target medium used for test of the network; medium is 2-D, and absorption is plotted on the z-axis (1.0 denotes nonabsorbing cells, 0.0 is a black body). Panel B: reconstruction obtained when the absorption is as is shown in 2A and the probabilities of scattering into each of the eight nearest neighbors of a cell are as shown in the inset. This result is correct mathematically, but physically inaccurate. Panel C: reconstruction obtained when the absorption is as is shown in 2A, scattering is isotropic, and the neural net is adjusted so the outer layers are desensitized during the first 1000 out of 1500 iterations.

A major problem left unaddressed at the time these results were first presented[4] is how in general we would get the information to supply to the neural net on where it should initially focus its attention. An important point is that this *a priori* information can not be derived from measurements of the same type, and made on the same occasion, as those which supply the primary input data to the image-reconstruction algorithm. For the neural net formulation, this means that if these types of algorithms are to enjoy more than the limited success they have shown so far, a major effort must be launched for the development of a rule-based data preprocessor.

Experience gained from development of such preprocessors for solution of other types of ill-posed problems with neural nets teaches that this type of endeavor should not be undertaken while there is any question of the intrinsic ability of neural nets to solve the problem. In this case, it means we should be certain beforehand that the patterns of light fluxes emitted from the surfaces of target media contain sufficient information to permit accurate image reconstruction if the

problems caused by ill-posedness could be eliminated. It is essential to perform measurements that afford the greatest possible degree of discrimination among different sites in the medium.

All our previous computational and experimental work supports the position that the optimal measurement scheme employs highly collimated sources and detectors, with the flux of emerging light measured as a function of direction as well as position. To address the question of whether successful network reconstructions could ever be expected to be possible, we turned to ideas we first considered several years ago[6,7] for examining the dependence of an absorber's impact on the source-detector separation and detector orientation, as is shown in Figure 3.

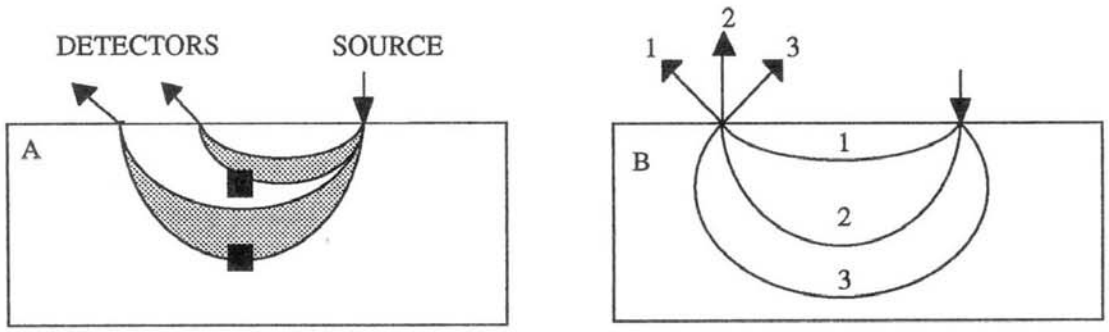

FIGURE 3 Sketch of proposed measurement scan, illustrating dependence of the impact of a localized absorber on the detector location and orientation. Panel A: the shaded areas joining the light source to the detectors are the region most heavily illuminated by the light passing from source to detectors. The shallow absorber, therefore, will have a much greater effect on the light flux seen by the near detector than on the far detector, and the deep absorber will have the opposite effect. In addition, if the source and detectors are moved simultaneously across the surface in either direction, the effect of both absorbers will rapidly diminish. Panel B: each numbered arc lies in the most heavily illuminated region for the corresponding detector. Deep absorbers have greatest effect on the light flux detected by 3. However, 3 also shows the least response to small changes in the position of the absorber.

In this paper, we present the results of our studies of the effect of localized absorbers on the angular distribution of light fluxes. The dependence of the region of a medium preferentially illuminated on the source-detector separation has been commented on and studied many times[8,9]. However, little effort has been expended on studying the effects of heterogeneities on the light exiting a medium at a single point as a function of direction. The reason why this should be so is not immediately apparent. It is, perhaps, due to practical difficulties in performing the measurements. In addition, diffusion theory, which is a popular framework for mathematically analyzing the distribution of light in dense scattering media, does not permit calculation of angular intensities or angular fluxes.

2.0 METHODS

2.1 2-D Relaxation Solver

The algorithm used in these calculations substitutes a finite difference equation for the continuous transport equation. An extensive mathematical description of the relaxation technique is given elsewhere[4]. The spatial, time, and direction coordinates all are discretized; it is assumed that all radiation in the medium has an interaction, either a scattering or an absorption, in each cell through which it propagates, and exactly once in each time-step.

For the particular calculations presented here, one unit of light energy was introduced into a single chosen border cell in each time-step (see Figure 4); its initial direction of propagation was along a normal to the boundary. At the same time, any light already in any cell of the medium propagated to that cell's eight nearest neighbors. The scattering was forward-directed, with the probabilities of light being deflected through an angle of 0°, 45°, and 90° from its initial

direction being 0.4, 0.4, and 0.2, respectively. The scattering was symmetric about 0°. This gives a net anisotropy factor of $g = 0.683$, with 0 probability of scattering through an angle greater than 90°.

The background material (white cells in Fig. 4) was nonabsorbing. Because the dimensions of the cells are the distance over which light has an average of one interaction with the medium (*i.e.*, one mean free pathlength (mfp)), it follows that $\Sigma_t = \Sigma_s = 1.0$. Σ_t and Σ_s are the macroscopic cross-sections for, respectively, all interactions and for scattering. In each relaxation calculation performed a small heterogeneous region was included, consisting of two adjacent cells (shaded cells in Fig. 4) with the same Σ_s as the background but a positive macroscopic absorption cross-section, Σ_a. Two different absorption strengths were used in the calculations. For the *strong absorber* case, Σ_a was chosen so that the light flux exiting the absorber in any direction in any time-step was 1% of what would have emerged if there were no absorption. For the *weak absorber* case, Σ_a was chosen so that the exiting light fluxes were 95% of what would have emerged if there were no absorption. These cases correspond to values for Σ_a of approximately 4.77 and 0.0484, respectively. In both cases, the effect of the absorber on the steady-state flux of light across the medium's boundary was calculated, for different absorber depths and different light source locations.

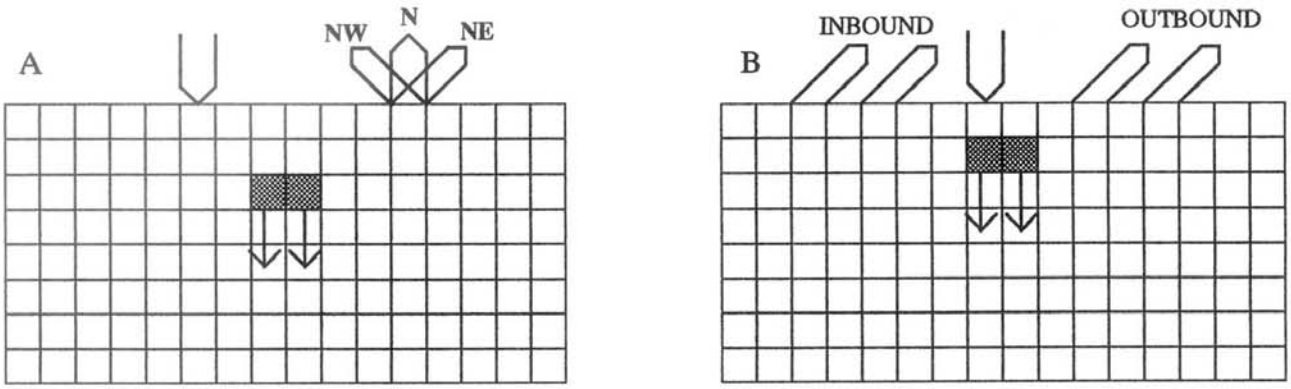

FIGURE 4 Sketch of medium, source and detector configurations used in 2-D relaxation calculations. Each cell is a square whose edge is one mfp. Radiation moves from a cell to its eight nearest neighbors in discrete time-steps, and is either scattered or absorbed in each cell it traverses. The 1-mfp cell width is the limit to the obtainable resolution in specifying the site at which light enters or leaves the medium. Panel A: all incident light begins its propagation in a single cell lining the boundary, traveling initially perpendicular to the surface. Light emerges from each boundary cell in three directions, called northwest (NW), north (N), and northeast (NE). Panel B: alternative classifications of fluxes of exiting light. Each of the fluxes shown is in the NE direction, but those to the left (west) of the source are designated "inbound" and those to its right (east) are called "outbound." These names describe the direction of the exiting light relative to the *source*, not to the surface.

The relaxation calculations were repeated until the amount of light energy either absorbed or escaping across the boundary in each time-step equaled the amount entering, and the fluxes of light both between cells and across the boundary did not change significantly between successive time-steps. The flux across the boundary, as a function of position and direction, was then recorded. The number of time-steps required for convergence depends on the number of cells in the medium. It was necessary to find a compromise between the objectives of making the medium large enough that the ouput would approximate the fluxes from a half-plane and small enough that the calculation would be completed in a reasonable time. This was done by first increasing the length and width of a homogeneous medium until the addition of more rows or columns produced no detectable change in output. The length and width were then reduced to obtain more rapid convergence, but only as long as the steady-state fluxes differed in no significant qualitative way from those obtained from the larger medium. The dimensions determined in this way were then used in all heterogeneous medium calculations. For every calculation in which an absorber was present, the initial state used was the steady-state flux distribution for the absorberless medium. As a consequence of this, convergence to the new steady state required many fewer iterations than if the calculation had begun from "scratch" with no light in the medium. A total of eighty calculations were carried out, each meeting the convergence criterion after approximately six iterations. These calculations collectively took about two minutes of run time; the object code was compiled QBASIC, running on an IBM PC.

2.2 3-D Monte Carlo Simulations

The Monte Carlo method[10] was used to study the effect of absorbers on light reflected from a 3-D dense scattering media. The physical model was more complex than that of the relaxation solver, in that the distribution of scattering angles was continuous and the distance light propagated between successive interactions with the medium was a random variable. For the simulations presented here, scattering was assumed to be isotropic. The essential properties of the model and simulation algorithm are shown in Figure 5. Detailed descriptions of these have also been given previously[1,2,11].

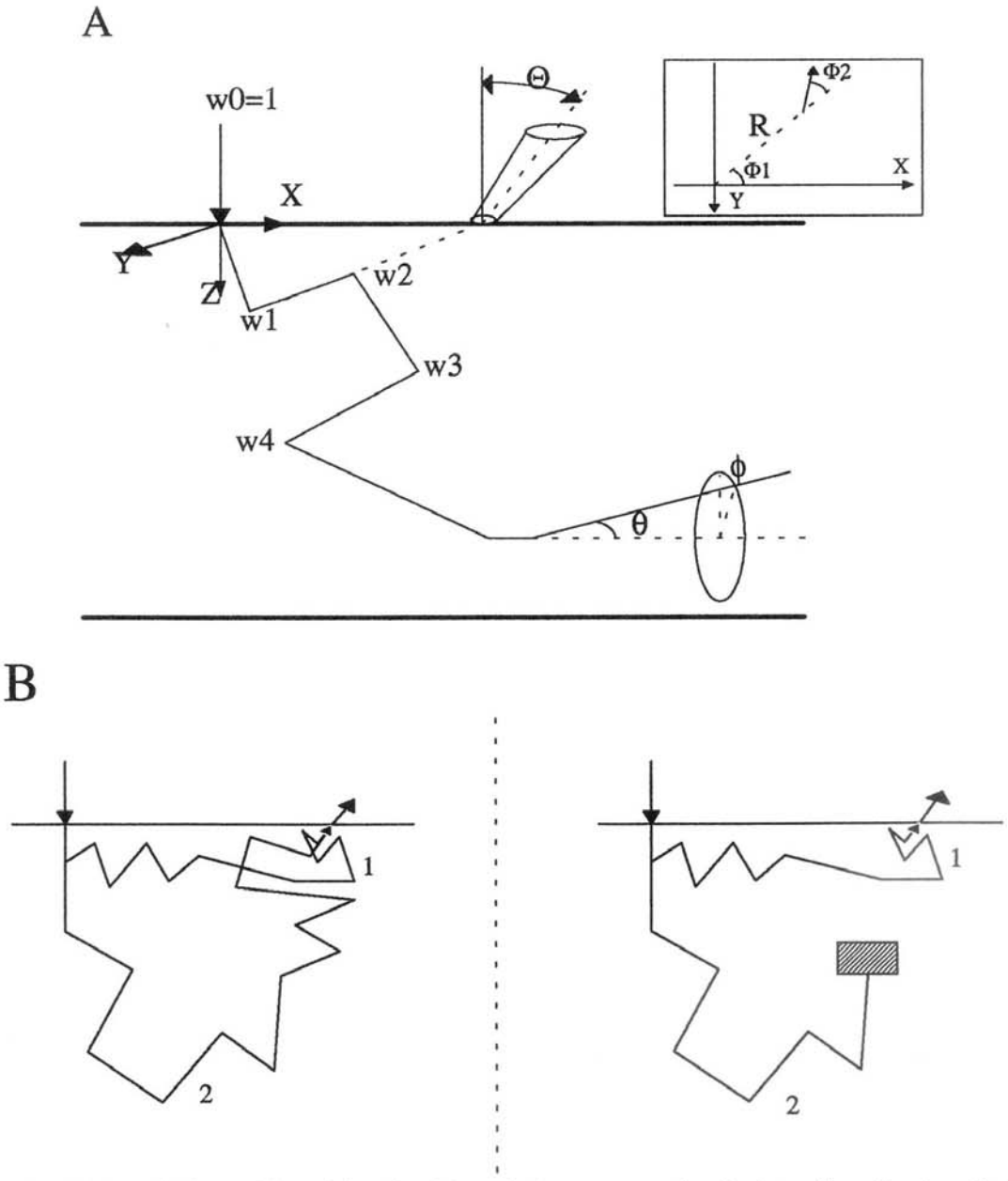

FIGURE 5 Sketch of Monte Carlo model used for simulation of photon propagation in three-dimensional media (reprinted from reference 5). Panel A: angles θ and ϕ describe deflection of photon from its previous direction upon scattering; ϕ is 0 when the plane determined by the pre- and post-scattering direction vectors is ⊥ medium's surface. w_n is a statistical weighting factor, the probability that the photon has neither escaped nor been absorbed. Θ, Φ_1, and Φ_2 describe the orientation of an emerging photon in the laboratory reference frame. Inset shows projection of exiting photon's path onto surface. Panel B: correlated sampling used as a noise reduction technique when calculating the effect of an absorber. Photons follow identical paths in both the homogeneous reference (left) and heterogeneous target (right) media, unless absorbed in the target medium. Photon 2 contributes to the illustrated detector on the left, but not on the right.

The absorber modeled was a black body with the shape of a "T."[12] Its total volume was 16 mfp^3, which was evenly divided between a 4x2x1 mfp^3 cap and a 2x2x2 mfp^3 stem; the shallowest point was 3 mfp below the surface. The source code for these simulations was a FORTRAN 77 program running on an IBM 4381 mainframe computer. Each simulation of three million photon histories took between twelve and twenty four hours. This variation is the result of a variable number of users sharing the machine; the true CPU times needed for the calculations, clearly much smaller than these "clock" times, are unknown.

2.3 Experimental Measurements

Using a red/NIR dye laser (Coherent model 599, Pyridin 2 dye) as the light source and a cooled CCD camera (Hamamatsu model C3140) as the detector, measurements of diffusely reflected and transmitted light were made about a cylindrical breast-tissue phantom[2,3]. The cylinder was filled with various concentrations of aqueous Intralipid® suspension; independent measurements[13] have shown that the highest concentration used, 2% lipid by volume, most closely matches the scattering and absorption properties of breast tissue. A glass rod (7 mm o.d, 5 mm i.d.) filled with a dilute India ink (1 mL ink, 7.5 mL water) was used as a heterogeneity. As shown in Figure 6, it could be placed into any one of seven receptacles in the cylinder, in each of which the rod is parallel to the cylinder axis.

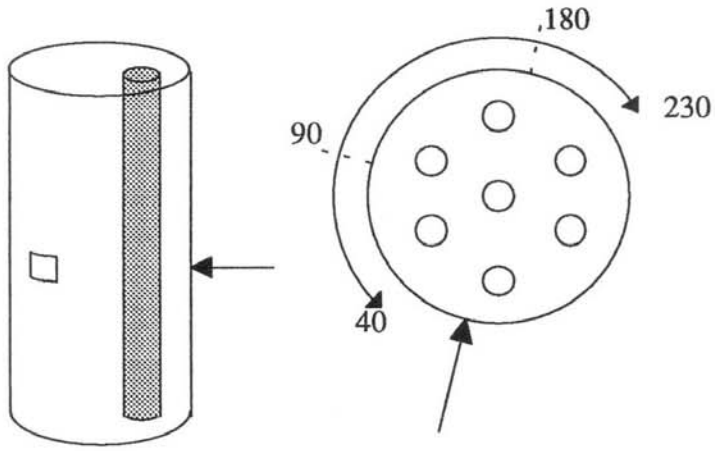

FIGURE 6 Sketch of medium used as breast-tissue phantom (reprinted from reference 5). Outside diameter of cylinder was ~8.7 cm, height of liquid column was ~35 cm. Panel A: arrow indicates point at which laser beam impinges on cylinder; to minimize end effects, this point was halfway between the ends of the liquid column. The dashed line indicates the boundary of the area seen by the detector. Panel B: end view of specimen, showing seven possible locations of the absorber relative to the light source (straight arrow) and cylinder axis. Curved arrows shows the arc through which the detector revolved about the specimen. The revolution steps were sufficiently small (10° central angle of cylinder) that there was considerable overlap between the areas photographed in adjacent camera locations. The result is that a single point on the surface may be seen from as many as seven different directions.

3.0 RESULTS

3.1 2-D Relaxation Calculations

An example of output from the relaxation solver is shown in Figure 7A. The quantity plotted on the y-axis is the outbound flux (ten units of light energy are sent into the medium in each time-step, and the fluxes are the number of units exiting the medium at a given location, in a given direction, per time-step) across the surface (see Fig. 4B); the cell index is plotted on the x-axis. For the calculations that produced this output, the strong absorber was present in the medium, always in cells in columns 7 and 8. The absorber was successively placed in rows 2 through 8, while the incident light always entered the medium in column 10. The forward-directed light scattering distribution is responsible for the "notch" in the

emerging light flux at the site of incidence; this flux would be considerably higher if there were a positive probability of light scattering through angles > 90°.

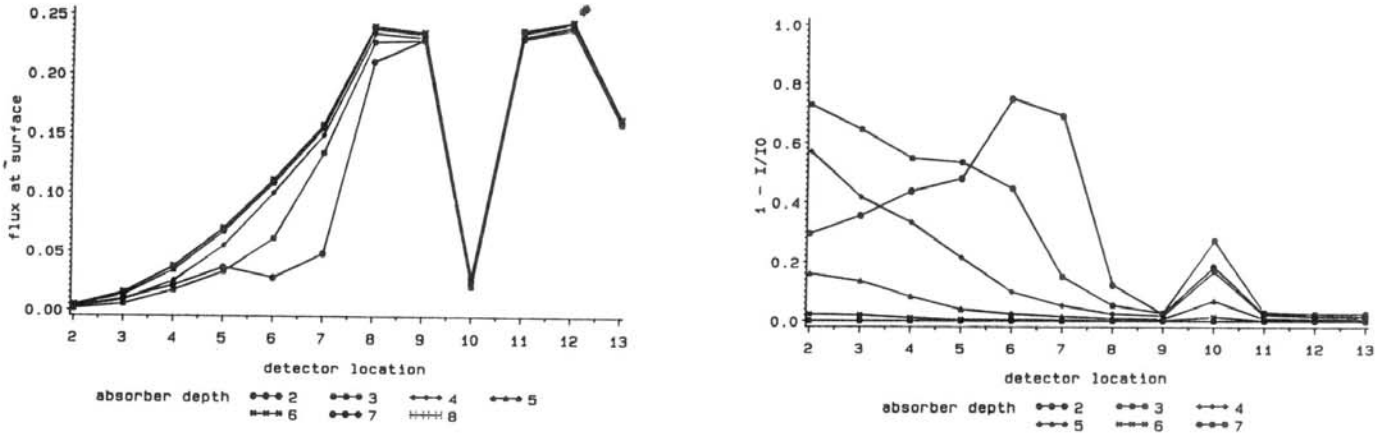

FIGURE 7 Effect of strong absorber on outbound flux across surface, 2-D relaxation calculations. Light enters medium in cell at row 1, column 10. All incident light initially moves ⊥ surface (south, see Fig. 4). Absorber is in columns 7 and 8, and in one of the rows in the range 2-8. It emits only 1% of the light energy that would have emerged from the same cells if there were no absorption there. Panel A: each curve shows outbound flux *vs.* column number for one value of absorber depth. Panel B: 1 - I/I_0, relative reduction in flux of light across surface, *vs.* column number for same set of data as shown in 7A. The deep notch at column 10 in 7A and the peaks in column 10 in 7B all are consequences of the scattering angle distribution used in these calculations, and would be greatly suppressed if scattering through angles >90° were permitted.

The effect of an absorber on light seen at different distances from the source, as a function of absorber depth, is shown in Fig. 7B. The quantity plotted on the y-axis, 1 - I/I_0, is the relative reduction in the flux of light across the surface as a consequence of placing the absorber in the medium. Inspection of the data presented in Fig. 7A shows that there was almost no change in the light flux at surface locations in columns 2-13 when the absorber moved from row 7 to row 8. Therefore, the impact of the absorber in row 8 on the flux across the surface in these columns is negligible, and accordingly the fluxes when the absorber was at this depth were used as I_0. The curves in 7B confirm the expectations illustrated in Fig. 3A: detectors near the source are affected most by absorbers near the surface, detectors farther from the source are affected more by deeper absorbers, and deep absorbers have a significant impact over a much larger area of the surface than shallow ones have.

For a given target medium, the depths of any absorbers present will be fixed. The information that must be used to estimate the strength, extent, and depth of absorbers is of the type shown in Figure 8. Here the strong absorber was fixed in columns 7 and 8 and row 4, and the source scanned across the surface, passing over the absorber in the process. The relative reduction in light flux across the surface is shown for each source location, and for both the outbound and inbound fluxes.

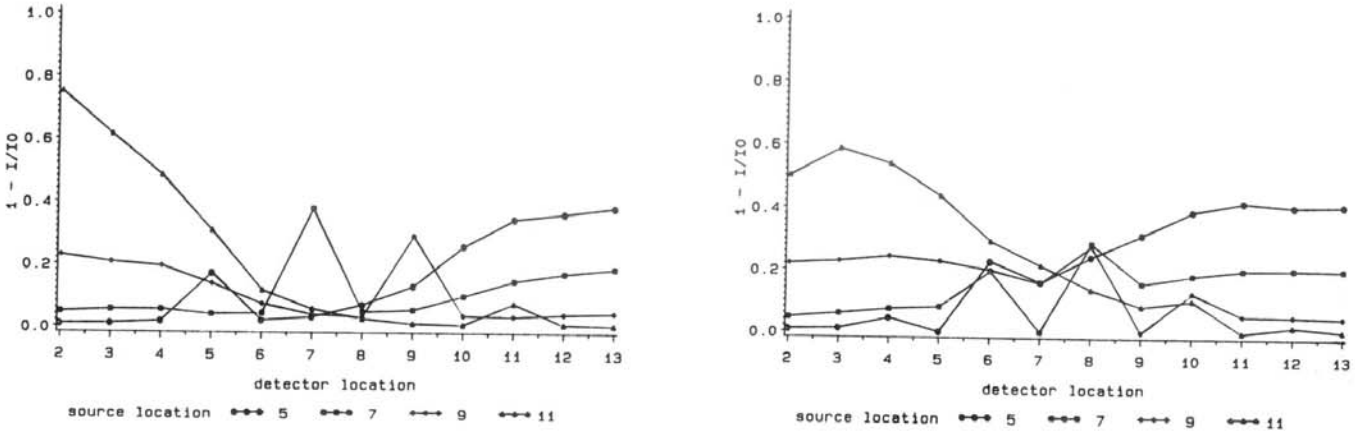

FIGURE 8 Effect of a fixed strong absorber on flux across surface, as a function of source location. Strong absorber is located in row 4, columns 7 and 8. Panel A: 1 - I/I_0 for outbound fluxes, four different points of incidence. As in Fig. 7B, peak at source location is due to the scattering angle distribution used. Panel B: 1 - I/I_0 for inbound fluxes, same four points of incidence. The relative reduction at the source location is here arbitrarily set to zero, as all emerging light at the source location is outbound. In this panel, the apparent dip in 1 - I/I_0 at column 2 when the source is at column 11 is probably an artifact caused by loss of significant figures in the recorded flux values for detectors far from the source.

Careful comparison of each curve in Fig. 8A to the corresponding curve in Fig. 8B confirms the expectation illustrated in Fig. 3B. At each source location, the effect of the absorber on the inbound flux one column away from the source is much greater than its effect on the corresponding outbound flux. While the outbound flux also experiences a large reduction at columns far from the source, its increase in 1 - I/I_0 with distance is initially much slower than that for the inbound flux. This result clearly shows the utility of directional measurements for estimating an absorber's depth.

As a test of the sensitivity of the emerging light to absorbers small in magnitude as well as size, the relaxation calculations were repeated with the weak absorber in row 2 and row 3. The weak absorber results shown in Figure 9 correspond to those in Fig. 7B and Fig. 8. By comparing Fig. 9A to Fig. 7B, it can be seen that while a given source-detector pair might be affected in exactly the same way by a weak, shallow absorber and a strong, deep one, the two cases

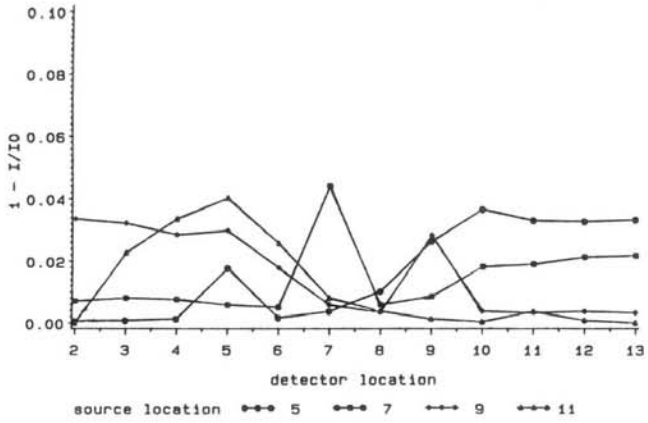

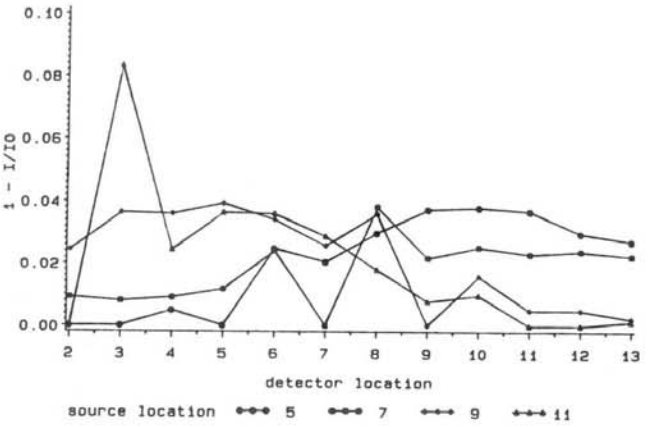

FIGURE 9 Effect of weak absorber on flux across surface, 2-D relaxation solver. Cells containing absorber are always in columns 7 and 8, and emit 95% of the light energy that would have emerged from them if there had been no absorption there. Panel A: 1 - I/I_0 for outbound flux, source is at column 10, absorber in either row 2 or row 3. Panel B: 1 - I/I_0 for outbound flux, absorber in row 3, source at column 5, 7, 9, or 11. As in Fig. 8B, some data points for the case of source at 11 are likely to be artifacts caused by loss of significant digits in the recorded values of I and I_0.

can readily be distinguished by examining 1 - I/I_0 as a function of source-detector separation. Comparison of corresponding curves in Fig. 9B and Fig. 9C shows the absorber affects inbound flux before outbound, just as in the strong absorber case. The weak absorber produces much smaller values of 1 - I/I_0, but these are still well within limits of detectability.

3.2 3-D Monte Carlo Simulations

When we progress from two to three dimensions for these simulations, the number of parameters needed to specify the location and orientation of light exiting the medium increases from two to four. In addition, since the directions are continuously distributed, the angles Θ and Φ_2 (see Figure 5A) can take on any values in the ranges 0° - 90° and -180° - 180°, respectively. The terms "inbound" and "outbound" are retained, however, to describe emerging light for which $|\Phi_2| > 90°$ and $|\Phi_2| < 90°$, respectively.

The contour plots shown in Figure 10 show 1 - I/I_0 at the surface of a slab medium with finite thickness and infinite length and width. Photons entered the medium at (0,0) along a normal to the surface. The detectors all had orientations given by $\Theta = 40°$ and $\Phi_2 = 0°$. That is, they were not parallel but exhibited radial symmetry about the source. In both cases the distance from source to the center of the absorber was the same, but the orientation of the absorber in the medium was different, as shown. This indicates that simple reflectance measurements can give information about the shape of a heterogeneity as well as its location, strength, and size.

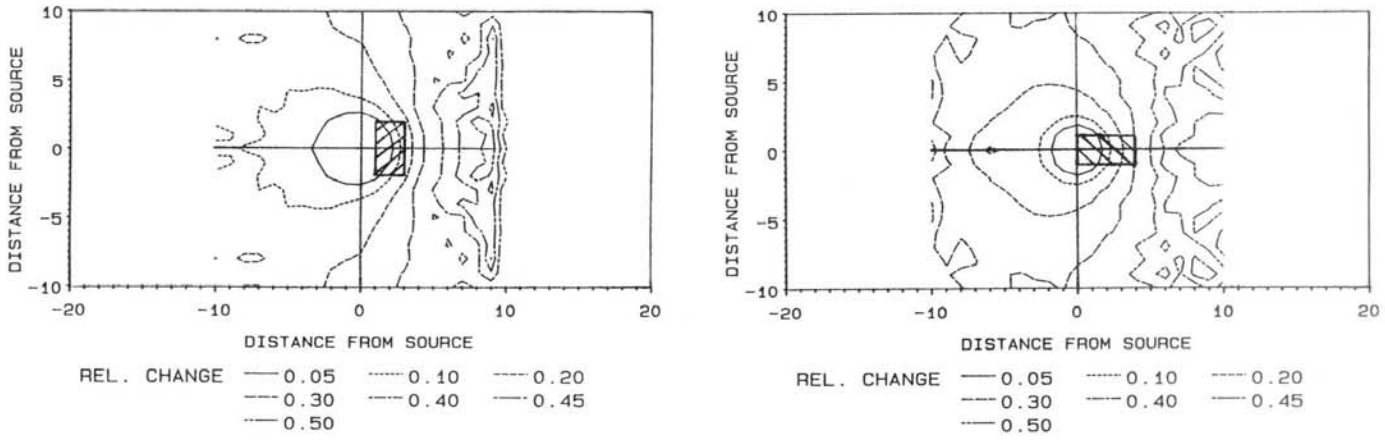

FIGURE 10 Contour plots of 1 - I/I_0 for 3-D Monte Carlo simulations. The reference medium was infinitely long and wide by 10 mfp thick, and had a homogeneous absorption cross-section of $\Sigma_a = .01\Sigma_t$. The "T" absorber was a black body whose cap and stem lay, respectively, between 3 and 4 mfp and between 4 and 6 mfp below the illuminated surface. The Monte Carlo model used for the simulation is shown in Fig. 5; as described there, correlated sampling was employed to simultaneously calculate I_0 and I.

The data presented in Figure 11 shows that the effect of localized absorbers on the flux across the surface of a 3-medium does not differ in any substantial manner from what is found in the 2-D case. In one set of simulations the source was initially located directly over the center of the absorber, then was moved away in one-mfp steps along the short symmetry axis of the absorber cap. The reduction in angular flux at points along the axis is shown in Fig. 11A for the case of detectors with the same orientation as those used to produce the data in Fig. 10. Unfortunately, data for the corresponding inbound fluxes are not available for comparison, but it is possible to show, in Fig. 11B, the effect of varying Θ and the orientation of the absorber. The 1 - I/I_0 curves plotted here all were obtained for the case of source located directly over the center of the absorber. The three pairs of curves show the absorber's effect on outbound flux at $\Theta = 10°$, 40°, and 80°. The solid curves show the effect at points along the long symmetry axis of the absorber, while the dashed curves show the effect at points along the short axis.

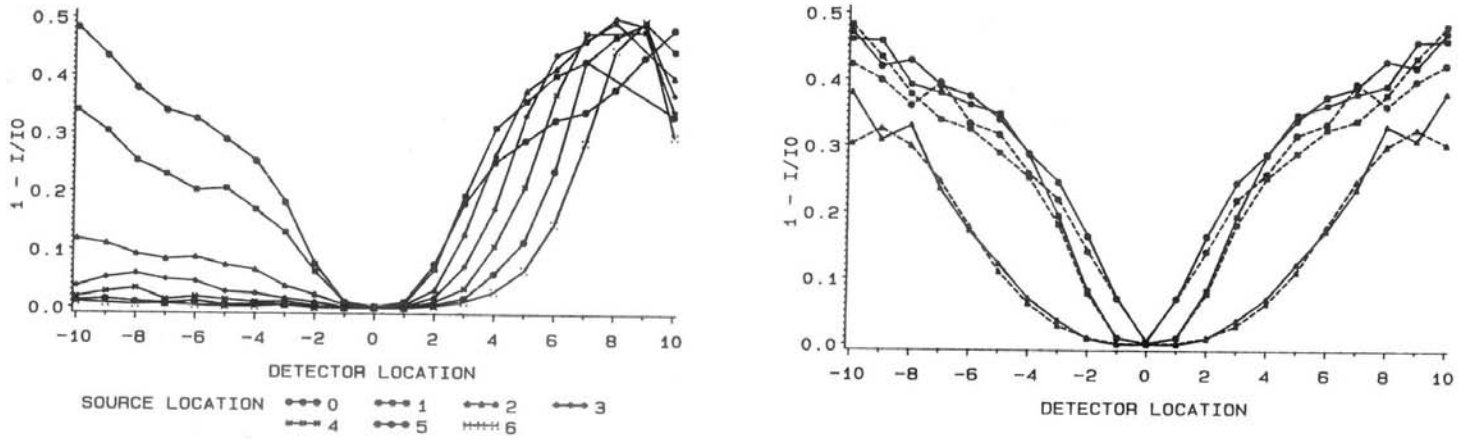

FIGURE 11 Effect of "T" absorber on angular flux across surface of slab medium. Panel A: source is initially located directly over absorber, then moved in one-mfp steps to the left along short axis of the absorber. Detector orientation is $\Theta = 40°$, $\Phi_2 = 0°$. Effect of absorber quickly becomes negligible at points to the left of the source, but remains large at points on the right. Panel B: source is located directly above absorber. Effect of absorber on flux in directions $\Theta = 10°$ (circle symbols), 40° (square symbols), 80° (triangle symbols); $\Phi_2 = 0°$. Solid curves show $1 - I/I_0$ at points over long symmetry axis, dashed curves at points over short symmetry axis.

3.3 Experimental Data

The seven curves shown in Figure 12 are plots of $1 - I/I_0$ obtained from experimental measurements as described in Methods (see Figure 6). There is considerable overlap between adjacent curve because of the 10° steps through which the camera revolved. Then many of the points on the cylinder are seen from four or five different directions, and the points at 11.9, 13.5, and 15.25 cm of the horizontal axis in Fig. 12 are replot in Figure 13 as $1 - I/I_0$ *vs.* angle α between the detected ray and the normal to the cylinder surface. The sketch in Figure 14 shows these three points on the cylinder, in relation to the point at which light entered the cylinder and to the location of the absorbing rod. Also shown in this figure are the limits of the angles from which a point on the cylinder could be seen in this experiment.

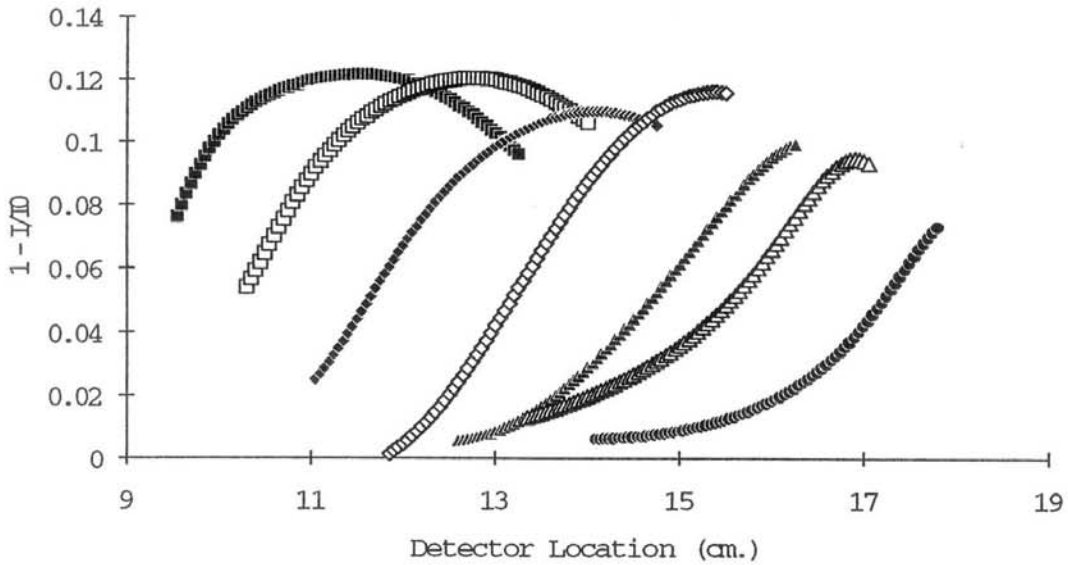

FIGURE 12 $1 - I/I_0$ from experimental measurements. The source and absorber locations were fixed; each curve corresponds to a different position of the camera about the cylinder.

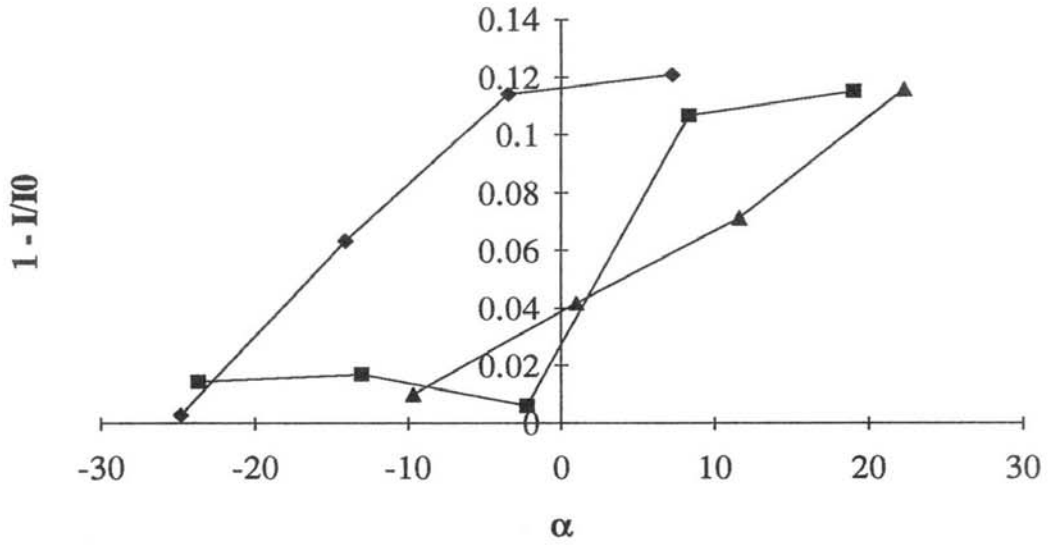

FIGURE 13 Replot of data from previous Figure, showing relative reduction in detected light caused by absorber *vs.* angle between detected light ray and normal to cylinder surface.

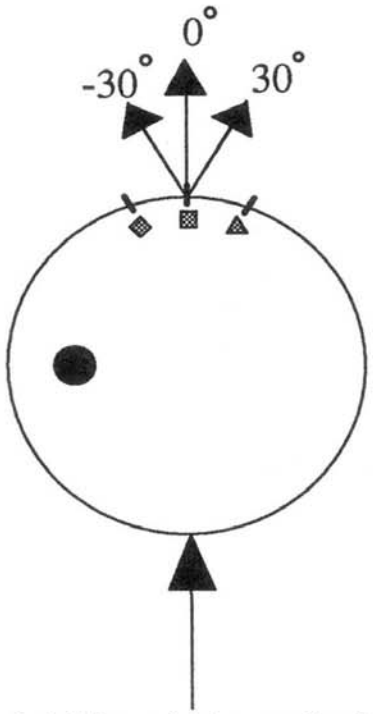

FIGURE 14 Sketch of three detector locations selected for replot in preceding Figure, in relation to absorber location and source location. Also shown is range of directions from which a point could be viewed in this experiment.

4.0 DISCUSSION

Unambiguous patterns were found in the distributions of detected light from dense scattering media in all the cases studied, by what really amounts to casual inspection of the detector readings. This assures us that sufficient information is present in the readings for a neural net algorithm to accurately reconstruct an image of such a medium if the dificulties caused by the problem's ill-posedness could be overcome. Therefore, the massive effort involved in developing a rule-based preprocessor for a neural net is fully justified.

It is of considerable interest that better localization of heterogeneities can be obtained by comparing the responses of detectors receiving light from a single point in different directions. Future developments of the neural net scheme will make deliberate use of the directional component of the pattern of emerging light. This is information that has invariably not been exploited before. We are confident the benefits obtained by doing so will more than outweigh the practical difficulties.

The rule-based preprocessor to be developed will attempt to derive accurate limits on the spatial distribution of NIR absorption by establishing correlations between this and data obtained from other imaging modalities, other noninvasive physical examinations, and basic knowledge of anatomy. An important goal of this is to reduce the problem of "clutter," in which the presence of small abnormalities is obstructed by nearby large, strongly absorbing, but perfectly normal structures. One can not expect to locate the former in a realistic test medium unless the structure and properties of the latter are known with very high accuracy.

5.0 REFERENCES

1) R.L. Barbour, H. Graber, R. Aronson, J. Lubowsky, "Model for 3-D optical imaging of tissue," Proc. 10th Annual International Geoscience and Remote Sensing Symposium (IGARSS), vol. II, pp. 1395-1399, 1990.

2) H.L. Graber, J. Chang, R. Aronson, R.L. Barbour, "A perturbation model for imaging in dense scattering media: derivation and evaluation of imaging operators," *Proc. SPIE Institute on Medical Optical Tomography*, 1993, in press.

3) H.L. Graber, J. Chang, J. Lubowsky, R. Aronson, R.L. Barbour, "Near infrared absorption imaging of dense scattering media by steady-state diffusion tomography," *Photon Migration and Imaging in Random Media and Tissue (SPIE Proceeding Series, vol. 1888)*, 1993, in press.

4) F.H. Schlereth, J.M. Fossaceca, A.D. Keckler, R.L. Barbour, "Imaging in diffusing media with a neural net formulation: a problem in large scale computation," *Physiological Monitoring and Early Detection Diagnostic Methods, (SPIE Proceeding Series, vol. 1641)*, pp. 46-57, 1992.

5) Y.H. Pao, *Adaptive Pattern Recognition and Neural Networks*, Addison-Wesley, 1989.

6) R.L. Barbour, H. Graber, J. Lubowsky, R. Aronson, "Monte Carlo modeling of photon transport in tissue," *Biophs. J.*, vol. 57, pp. 381a-382a, abst. no's 599-600, 1990.

7) R.L. Barbour, H.L. Graber, R. Aronson, J. Lubowsky, "Determination of macroscopic optical properties of multilayer random media by remote sensing," *Time-Resolved Spectroscopy and Imaging of Tissue, (SPIE Proceedings Series, vol. 1431)*, pp. 52-62, 1991.

8) R.A.J. Groenhius, H.A. Ferwerda, J.J. Ten Bosch, "Scattering and absorption of turbid materials determined from reflection measurements. 1. Theory," Applied. Optics, vol. 22, pp. 2456-2462, 1983.

9) G.H. Weiss, R. Nossel, R.F. Bonner, "Statistics of perturbation depth of photon re-emitted from irradiated tissue," *J. Modern Optics*, vol. 36, pp. 349-359, 1989.

10) M.H. Kalos, P.A. Whitlock, *Monte Carlo Methods, volume I: Basics*, John Wiley & Sons, New York, 1986.

11) H.L. Graber, R.L. Barbour, J. Lubowsky, R. Aronson, B.B. Das, K.M. Yoo, R.R. Alfano, "Evaluation of steady-state, time and frequency- domain data for the problem of optical diffusion tomography," *Physiological Monitoring and Early Detection Diagnostic Methods, (SPIE Proceeding Series, vol. 1641)* pp. 6-20, 1992.

12) R.L. Barbour, H.L. Graber, R. Aronson, J. Lubowsky, "Imaging of subsurface regions of random media by remote sensing," *Time-Resolved Spectroscopy and Imaging of Tissue, (SPIE Proceedings Series, vol. 1431)*, pp. 192-302, 1991.

13) I. Driver, J.W. Feather, P.R. King, J.B. Dawson, "The optical properties of aqueous suspensions of Intralipid, a fat emulsion," *Phys. Med. Biol.*, vol. 34, pp. 1927-1930, 1989.